Argo array observation of ocean heat content changes induced by tropical cyclones in the north Pacific

Jong Jin Park,[1] Young-Oh Kwon,[1] and James F. Price[1]

[1]   In situ observations from the autonomous Argo float array are used to assess the basin-averaged ocean heat content change driven by tropical cyclones (TCs) in the North Pacific for 2000–2008. A new statistical approach based on pairs of profiles before and after each TC event is employed here to estimate the near-surface and subsurface heat content changes. Previous studies have suggested a dominant role for vertical mixing in the SST cooling response during TC passages. The Argo float observations show that, under strong TCs (greater than or equal to category 4), the subsurface warming expected from vertical mixing occurs with comparable magnitude to near-surface cooling. However, when weak TCs (less than or equal to category 3, which are about 86% of the total of TCs) were also considered, the subsurface warming was not detectable in the Argo data set, while near-surface cooling was still significant. Therefore, these results suggest that air-sea heat exchange and (upward) vertical advection likely play a somewhat greater role in the case of weak TCs. Additionally, Argo observations suggest that the restoring time scale of the near-surface heat content is greater than 30 days, which may be compared with the approximately 10 day time scale for the restoration of sea surface temperature. The mixed layer temperature and mixed layer depth evolutions also estimated from Argo data support the notion that only a thin surface layer is restored quickly to pre-TC conditions, while the rest of the cooled near-surface layer retained the TC-induced response for a good deal longer.

Citation: Park, J. J., Y.-O. Kwon, and J. F. Price (2011), Argo array observation of ocean heat content changes induced by tropical cyclones in the north Pacific, *J. Geophys. Res.*, *116*, C12025, doi:10.1029/2011JC007165.

1.   Introduction

[2]   A cold wake in the sea surface temperature (SST) is perhaps the most outstanding feature of the upper ocean response to a tropical cyclone (TC) [e.g., *Cornillon et al.*, 1987]. It has been observed that SST and near-surface cooling under a strong TC is generally accompanied by warming in the subsurface, shown schematically in Figure 1a [e.g., *Price*, 1981; *D'Asaro et al.*, 2007]. This implies that SST cooling under a strong TC is caused primarily by vertical mixing associated with strong TC winds. *Emanuel* [2001] proposed that the near-subsurface cooling (the red hatched area ΔH_A in Figure 1a) would be restored by air-sea heat fluxes toward the pre-TC state within roughly a few weeks after a TC passage (shown schematically in Figure 1b) while the subsurface warming (the blue hatched area ΔH_B in Figures 1a and 1b) would persist for a longer time. The net result of TC-induced vertical mixing and recovery would thus be an ocean heat uptake (OHU) compared with no TC. He further hypothesized that the TC-induced OHU would

be advected poleward as a part of the meridional ocean heat transport (OHT). Thus an interannual variation in the number or intensity of TCs would cause an interannual variation in OHT and provide a long-period, ocean–atmosphere coupling.

[3]   Several studies have estimated the globally integrated TC-induced OHU using various kinds of remote and climatological observations [*Sriver and Huber*, 2007; *Sriver et al.*, 2008; *Jansen et al.*, 2010]. *Sriver and Huber* [2007] assumed that ΔH_B equaled the near-surface heat loss, ΔH_A, as would hold if vertical mixing was the only cooling mechanism. Then, they estimated the near-surface heat loss (ΔH_A) from SST cooling (ΔSST) and climatological vertical temperature profile. For each TC-affected location, they assumed that the pre-TC temperature profile would be the same as the climatology before the TC and that the mixed layer temperature (MLT) for the poststorm profile was colder by ΔSST from the climatology. From this they estimated that the TC-induced OHU was about 0.48 PW, globally, and for the period 1998–2005. This estimate of OHU is comparable to Emanuel's original estimate [*Emanuel*, 2001] and is a significant fraction of the ocean's overturning heat transport at subtropical latitudes. There are some aspects of this method that could result in an overestimate of the TC-induced heat loss in the near-surface ocean, ΔH_A and thus

---

[1]Physical Oceanography Department, Woods Hole Oceanographic Institution, Woods Hole, Massachusetts, USA.
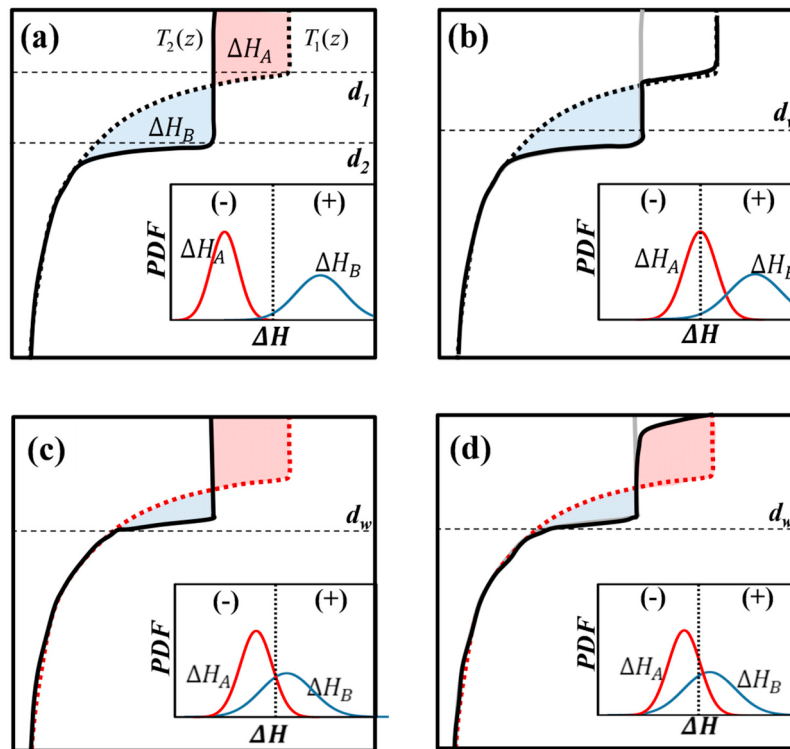
Figure 1. Schematic diagrams for the pair of temperature profiles before and after a tropical cyclone (TC) event. The black dashed line ($T_1(z)$) is a pre-TC profile, and the black solid one ($T_2(z)$) is a post-TC profile. The red cross-hatched area indicates the heat content change in the near-surface ocean (ΔH_A), and the blue hatched area indicates the excessive heat gain in the subsurface (ΔH_B). The red and blue curves within the small boxes are schematics of the probability density functions of the heat content changes generated by the types of the profile change in the respective panels. Gray dashed lines corresponding to d_1, d_2, and d_w indicate the mixed layer depths of pre-TC profile, post-TC profile, and following winter, respectively. The OHU hypothesis assumes the case represented by (a) temperature profile change dominated by vertical mixing due to TC wind immediately after a TC, which is a typical case with strong TC, and (b) post-TC profile reflecting the near-surface cooling completely restored by the air-sea heat flux. The gray solid line indicates the immediate post-TC profile from Figure 1a. The Argo observation in this study can be summarized by (c) the immediate post-TC profile produced by less penetrative mixing due to majority of weak TC (gray line; $\Delta H_A > \Delta H_B$ even initially) and (d) post-TC profile showing only restoration in the surface thin layer; therefore, the near surface is only partially restored rapidly. Note that ΔH_B may still be smaller than the amount of ΔH_A. There is a slight positive shift in PDFs of ΔH_B in Figures 1c and 1d.

heat gain in the subsurface, ΔH_B. The vertical mixing is not the only process causing TC-induced surface cooling. Along with vertical mixing, upwelling near the track of a TC and surface heat loss to the atmosphere will also lead to upper ocean cooling, though without causing subsurface warming. Studies that ignore cooling processes other than vertical mixing may thus yield an overestimation of the TC-induced OHU.

[4] *Jansen et al.* [2010] repeated the calculation of *Sriver and Huber* [2007] using different ocean temperature climatology and satellite data sets, and estimated OHU to be 0.58 PW, which is roughly consistent with the previous studies. However, they pointed out that as the mixed layer (ML) deepened in winter (as shown schematically with d_w in Figures 1b and 1c), some portion of the subsurface warm anomaly would likely be reentrained into the ML and released back to the atmosphere locally. When this seasonal cycle effect was considered, they estimated that the long-

term OHU (that survived an annual cycle) was reduced to 0.14 PW, or only about 25% of the earlier estimates that ignored the seasonal cycle. Recent studies and findings [*Jansen et al.*, 2010; see also *Sriver et al.*, 2008; *Pasquero and Emanuel*, 2008] thus suggest that TC-induced OHU might not have as large an impact upon the OHT as first conceived and estimated. What has not yet been reported, however, is an estimation of OHU based upon in situ temperature measurements.

[5] Autonomous Argo floats have been collecting temperature and salinity profiles over the global ocean for about 10 years and including under the severe weather conditions that accompany TCs (http://www.argo.ucsd.edu/). At present, there are more than 3000 floats distributed over the global ocean and most of them measure a temperature and salinity profile over the upper 2000 m. *Kwon* [2003] proposed a method to estimate the upper ocean response to TCs by comparing Argo profile pairs before and after TCs in the
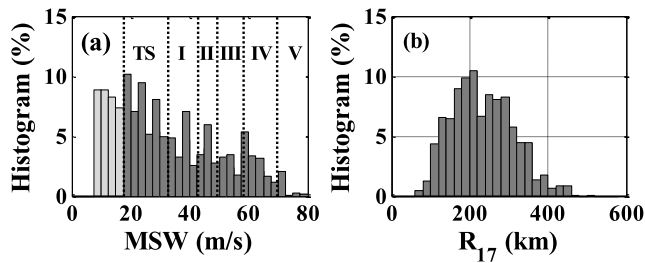
Figure 2. (a) Histogram of maximum sustained wind (MSW) of TCs (>17.5 m/s) used in this study. Light gray bars show frequencies of TCs with MSW of less than 17.5 m/s, which are excluded in our analysis. The TCs of weaker than category 1 (≤42.5 m/s) occupy 65%, and stronger than category 4 (≥58 m/s) comprise 14%. Dotted lines divide MSWs according to the Saffir–Simpson hurricane scale. (b) Histogram of radius of 34 knots (17 m/s), R_{17}. Mean value of the radius is about 210 km.

North Atlantic. *Park et al.* [2005] and *Liu et al.* [2007] followed his method to estimate the mixed layer responses to TCs in the North Pacific. However, the observed changes from the Argo profile pairs during the TC events inevitably contain noises associated with background variability independent of the TC-induced responses. Sparse sampling in time and space for the Argo profiles aggravates this contamination, as *Park et al.* [2005] pointed out. However, none of the previous studies attempting to utilize Argo profiles statistically [e.g., *Kwon*, 2003] as well as using individual Argo profile pairs [e.g., *Shi and Wang*, 2011] have considered the confounding background variability for their estimates of the TC-induced ocean response.

[6] In this paper, by taking advantage of the extremely extensive Argo data set, we attempt to sort the TC-induced response from the ambient or background variability present in all upper ocean observations. A specific goal will be to quantify the TC-induced OHU. A new statistical method will be employed to estimate the basin average, near-surface and subsurface ocean responses to TCs in the North Pacific basin using in situ Argo profile observation. Details on the new method and the Argo profiles are in section 2. Results are presented in section 3, and summarized and discussed in section 4.

2. Estimating the Upper Ocean Response to Tropical Cyclone Using Argo Profiles

2.1. TC Trajectory Data

[7] The best track data from the U.S. Joint Typhoon Warning Center (http://www.usno.navy.mil/JTWC) were used to locate the Argo profiles near the TC trajectory. Note that the only storms with maximum sustained wind (MSW) of stronger than 17.5 m/s were regarded as TCs in this study, which comprised about 75% of the total best track data between 2000 and 2008 (Figure 2a). The information on storm structure from this database such as radius of 34 knot (~17 m/s) wind (R_{17}), which generally marks the outer radius of a TC [*Dean et al.*, 2009], and radius of maximum wind (RMW) was used to define the area under TC influence (Figure 2b).

2.2. Sampling Criteria for the Argo Profile Pairs

[8] For the tropical and subtropical region of the western North Pacific (0°~30°N, 120°E~180°), there were about 42,600 quality controlled Argo temperature profiles from the Global Argo Data Center for the period 2000 to 2008 (Figure 3). We selected the Argo data only with "good" and "probably good" flag and then manually removed the left-over erroneous data. (Details about the delayed mode QC and Argo data flags can be found in work by T. Carval et al. (Argo data user manual version 2.3, 2010, http://www.argo.net) and *Park and Kim* [2007].) The Argo profiles before and after a TC event were then paired to calculate the heat content changes induced by TC. This data set was sorted to retain only those profile pairs that fit four sampling criteria appropriate to a TC response study: (1) For water depth, we have retained data only where the water depth was greater than 1000 m in order to avoid coastal regions. (2) For the distance from a TC track, both of the Argo profiles must have been within the search radius, R_{17}, to be retained (Figure 2b). This histogram of R_{17} is comparable to that from North Atlantic
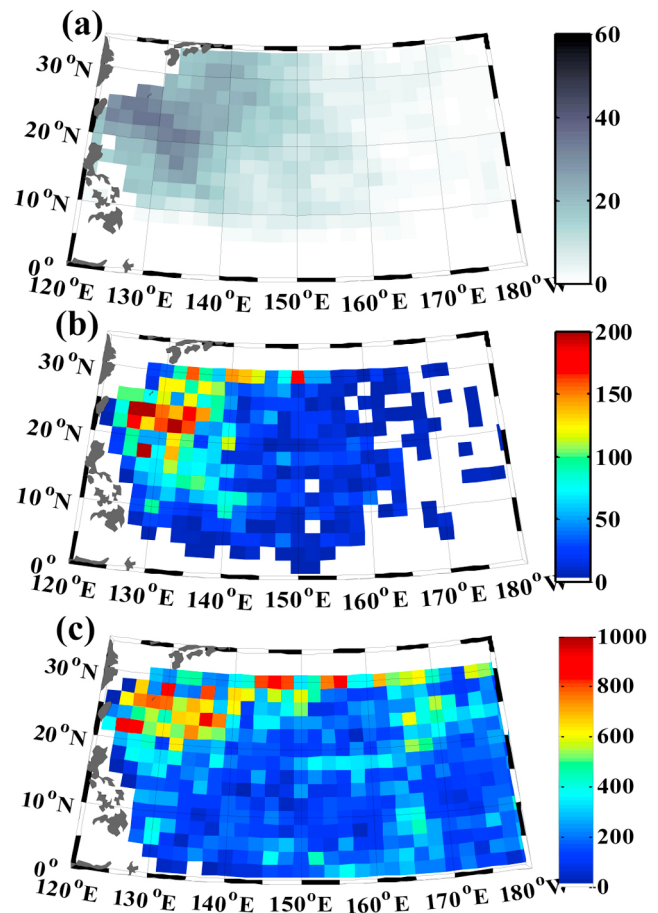

Figure 3. (a) Number of TCs with maximum sustained wind stronger than 17.5 m/s in each 2° × 2° region during 2000–2008. R_{17} (radius of 34 knot wind) swath is assumed from each storm track. (b) Number of Argo profile pairs for TC event. (c) Number of Argo profile pairs without TC event (apart from more than 15 days before and 60 days after TC events and outside of 400 km swath away from the tracks).
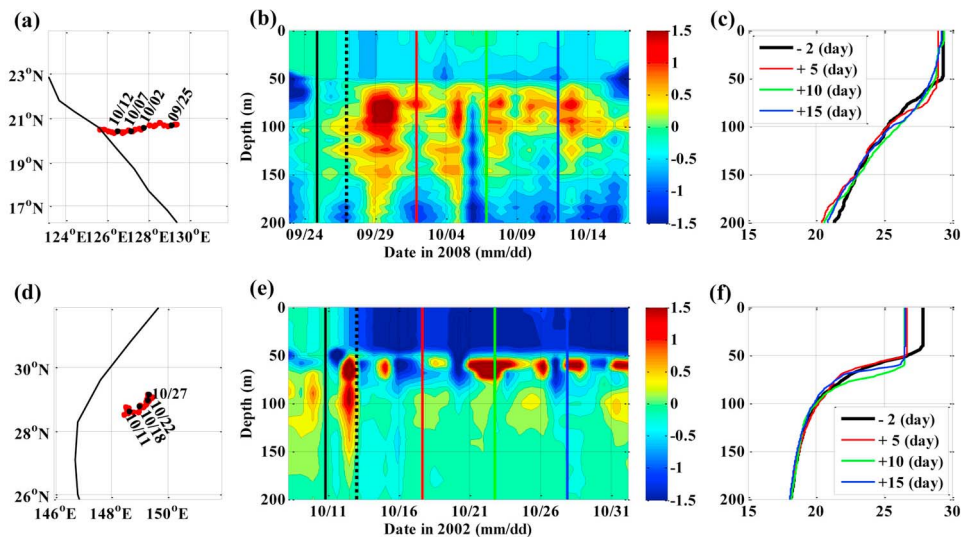
Figure 4. Upper ocean temperature response to TCs measured by Argo floats with unusually short profiling interval. (a–c) Float ID 5901578 (profiling interval of 24.0 h) under a strong TC (maximum sustained wind of 69 m/s, category 4). (d–f) Float ID 290240 (profiling interval of 20.5 h) under a weak TC (maximum sustained wind of 25 m/s, category TS). Figures 4a and 4d are the locations of profiles used in Figures 4b and 4e (red dots), with the locations of profiles in Figures 4c and 4f (black dots). The solid lines denote the TC tracks. Figures 4b and 4e are the temporal section of temperature anomalies (T − T_{ref}). Black lines indicate timings of the reference temperatures (T_{ref}) regarded as before-TC profiles, and all the colored lines including black ones indicate timings of profiles shown in Figures 4c and 4f. Dotted lines denote the timings of TC passages. Figures 4e and 4f are the temperature profiles 2 days before (black), 5 days after (red), 10 days after (green), and 15 days after (blue) the TC passages.

TCs in terms of its shape and range [*Dean et al.*, 2009]. The results we describe here are not sensitive to the choice of spatial search radius (Figure S1 in the auxiliary material versus Figure 6).[1] In addition, the distance between the paired profiles must have been less than 200 km to minimize the anomalies due to background spatial ocean variability. (3) For the temporal window, the pre-TC profile must have been obtained no more than 10 days before the TC passage. We have experimented with three different criteria for choosing the post-TC profile, 0–10 days, 10–20 days, and 20–30 days after the TC passage. The difference among these windows is used to estimate the time evolution of heat content changes. (4) Finally, for the float identity, the profile pairs must be from the same float to avoid duplicate usage of profiles and float-to-float calibration differences.

[9] Despite all of these (necessary) sampling criteria, a significant number of Argo profile pairs were found (Figure 3b). For comparison, the spatial distribution of TCs alone is shown in Figure 3a, and the distribution of non-TC Argo profile data is in Figure 3c. As expected, the northwestern part of the western North Pacific domain is most frequently affected by TCs. It is fortunate that the profile pairs from TC and non-TC periods have very similar geographical distributions, and so we have assumed that statistics of background variability in non-TC periods is the same as that in TC periods (more on this in section 2.3.). In addition, the sampled Argo profile pair distributions have similar spatial patterns to that of the TC distribution. From

this we infer that the Argo profiles analyzed here are likely to be representative of the basin-scale averaged TC response in the western North Pacific.

2.3. Statistical Approach

[10] Even with the above search criteria in place, the difference between the pre-TC and post-TC temperature profiles inevitably contains not only the TC-induced responses but also significant background variability that is independent of the TC passage, e.g., the seasonal cycle (which has a large signal in this analysis), internal waves, mesoscale fronts, and eddies. This "background" variability is significant even when the TC response has a larger spatial scale than the spatial search radius. We are not aware of any method that would be suitable for removing this background variability (noise for our purpose) directly from profile pairs to leave only the TC-induced response. Hence, we have attempted to separate the TC-induced signal using a statistical approach.

[11] Examples of this background variability and the resulting contamination of the TC-induced signal are shown in Figure 4 for a strong (Figures 4a–4c) and a weak (Figures 4d–4f) TC event. These particular floats measured temperature profiles once per day, while typical Argo floats sample one profile every 10 days. In such high temporal resolution data, we may separate TC-induced heat content changes, near-inertial oscillation, and ocean background variability, on the basis of their distinctive time scales [e.g., *Sanford et al.*, 2007]. The expected near-surface cooling and subsurface warming are evident during both of these TC events. However, there is also clearly complex background
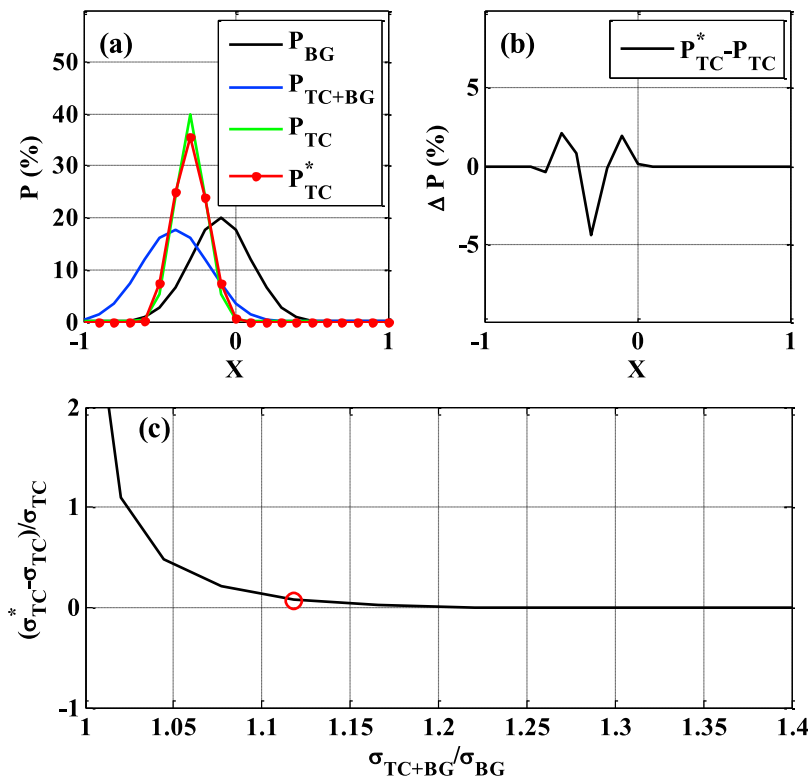
Figure 5. Sensitivity test of Lucy-Richardson deconvolution method using Gaussian PDFs. (a) An example of the test. Black line is a PDF of background (P_{BG}). Green line is a target PDF for the response to TC (P_{TC}). Blue line is the convolution of P_{BG} and P_{TC}, i.e., P_{BG+TC}. Red line with dots is the estimated target PDF ($P_{TC}*$) using the deconvolution of P_{BG+TC} and P_{BG}. (b) Difference between the true (P_{TC}) and the estimated ($P_{TC}*$). (c) Dependency of error in the width (standard deviation σ) of deconvolved PDF as a function of the ratio between the input widths of P_{BG+TC} and P_{BG}. Open red circle presents where the examples (Figures 5a and 5b) are placed ($\sigma_{TC+BG}/\sigma_{BG}$. = 1.12, $\sigma_{TC}* - \sigma_{TC}/\sigma_{TC} = 0.07$).

variability and an inertia-gravity wave response to TC (Figures 4b and 4e). In the much more typical 10 day sampled Argo profiles, as mimicked by subsampling the high-frequency samples in Figures 4c and 4f, the various kinds of background variability are practically inseparable. Therefore, a robust statistical approach is necessary to extract the TC response.

[12] Under the assumption that the profile pairs are randomly sampled and that instrumental noise is homogeneous, we have estimated the probability density function, P, of the upper ocean heat content change, x, in response to TC. The observed x is in practice a combination of TC-induced response, x_{TC}, and background variability, x_{BG}, that is presumed to be independent of TC. That is, the measured x is presumed to be a linear sum of x_{TC} and x_{BG}. The probability density function $P(x)$ can then be written as $P(x) = P(x_{TC} + x_{BG}) = \int P_{TC}(c)P_{BG}(x - c)dc$, according to probability theory, provided that x_{TC} and x_{BG} are independent variables, and $P_{TC} \equiv P(x_{TC})$, and $P_{BG} \equiv P(x_{BG})$ [*Hirschman and Widder*, 1955]. For instance, let's consider that x_{TC} and x_{BG} are positive integers, and the case $x_{TC} + x_{BG} = 3$. The probability P_{TC+BG} can be written as the sum $P_{TC}(1)P_{BG}(2) + P_{TC}(2) P_{BG}(1) + P_{TC}(3)P_{BG}(0) + P_{TC}(0)P_{BG}(3)$. When x_{TC} and x_{BG} are extended to real numbers, the probability $P_{TC+BG}(3)$ can be expressed as $\int P_{TC}(c)P_{BG}(3 - c)dc$. Therefore, the probability density function (PDF) obtained from Argo

profile pairs sampled during TC events (P_{TC+BG}) can be written as a convolution between the PDF of the storm-induced response (P_{TC}) that we seek, and the PDF of the background variability (P_{BG}) that we can estimate by using the (very large number of) Argo profile pairs that fall well outside the TC response sampling windows noted above. The estimated P_{BG} is assumed to be the background variability during TC events on the basis of similarity of the data distributions shown in Figures 3b and 3c. The mean value of x_{TC} may be computed by straightforward averaging; by solving for the probability density function $P_{TC}(x)$, we can also make an estimate of the statistical significance of the mean.

[13] The deconvolution is solved by the Lucy–Richardson algorithm, an iterative procedure often used in image processing to recover a blurred image [*Biggs and Andrews*, 1997]. The algorithm is tested here using artificially generated Gaussian PDFs (Figure 5). This example suggests not only the robustness of the algorithm, but also small uncertainty in the method itself. Assuming PDFs with Gaussian shapes, the error of P_{TC}^* (an estimate of P_{TC}) depends upon the ratio of widths of P_{BG} and P_{TC+BG}; the error is independent of the mean distance between the PDFs. If the width of P_{TC+BG} is similar to that of P_{BG}, P_{TC} would be close to a Delta function and the error of the deconvolved P_{TC}^* becomes greater. As the ratio gets larger than 1, error of the deconvolution rapidly decreases, and is ~10% for a ratio of 1.1 (see
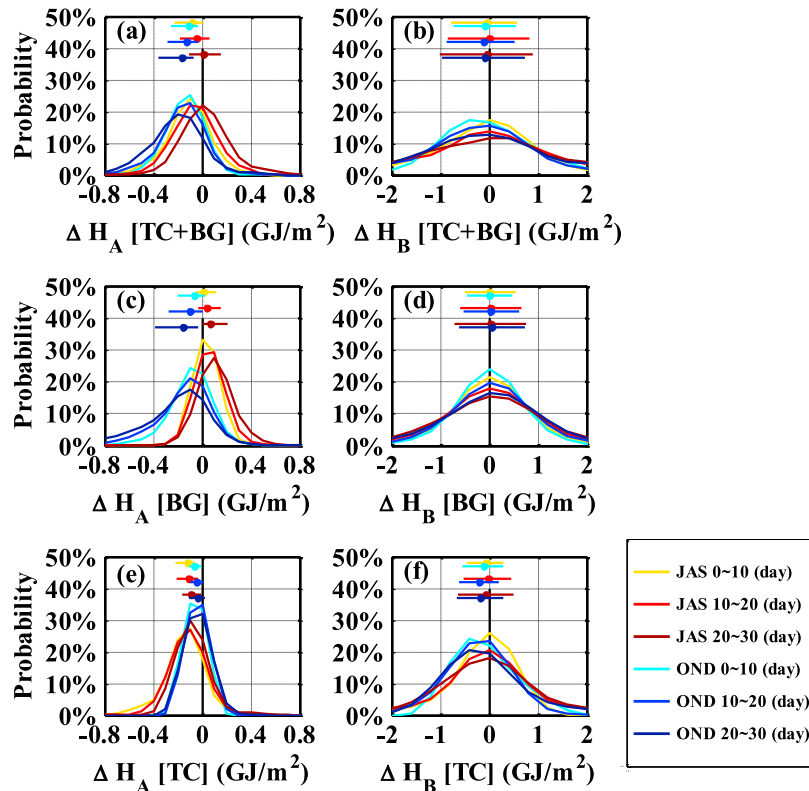
Figure 6. Probability density functions of (left) near-surface (ΔH_A) and (right) subsurface (ΔH_B) heat content changes observed from the Argo profile pairs. The warm colors are for the warming season (July–September), and cool colors are for the cooling season (October–December). In addition, different colors indicate different time windows after TC passage for the after-TC profiles. The dots and horizontal lines show means and 25%–75% percentile ranges of corresponding PDFs. (a and b) PDFs of ΔH_A and ΔH_B from the profile pairs during TC event which contain not only TC-induced responses but also background variability. (c and d) PDFs of ΔH_A and ΔH_B from the profile pairs during non-TC periods in which only the background variability is present. (e and f) PDFs of ΔH_A and ΔH_B obtained from deconvolution of Figures 6a and 6b and Figures 6c and 6d, which are estimated TC-induced responses.

Figure 5c). The ratio of widths between P_{TC+BG} and P_{BG} obtained from Argo observation typically ranges between 1.15 and 1.35, implying that the overestimation of the width of P_{TC}^* should be less than 5%. It is notable that the accuracy of the deconvolution is not sensitive to PDF skewness ($\int ((x - m)^3/\sigma^3)P(x)dx$, where m is mean and σ is standard deviation) within the range of the observational PDFs (from -89 to $+10$) (not shown).

2.4. Definition of Near-Surface and Subsurface Heat Content Changes

[14] Our focus in this paper is on the near-surface heat content change ΔH_A and subsurface heat content change ΔH_B (Figure 1). These are calculated from the individual profile pair as $\Delta H_A = c_p \rho_0 \int_{z_c}^{0} \Delta T(z)dz$ and $\Delta H_B = c_p \rho_0 \int_{-400}^{z_c} \Delta T(z)dz$, where $\Delta T(z) = T_2(z) - T_1(z)$. $T_1(z)$ and $T_2(z)$ are temperature profiles before and after TC event, respectively, ρ_0 is the water density ($= 1024$ kg/m³), and c_p is the heat capacity ($= 4186$ J/kg°C). z_c is the depth at which pre-TC and post-TC profiles intersect, i.e., $T_2(z) - T_1(z) = 0$, when an intersection is found between the mixed layer depths (MLDs) of pre-TC and post-TC profiles, i.e., if

$MLD_2 < z_c < MLD_1$. This is expected to hold when vertical mixing is the dominant process causing temperature change, as shown schematically in Figure 1a (see also an example from an actual Argo profile pair in Figures 4c, 4f and 8c). This case has been assumed in all of the previous studies on the TC-induced OHU.

[15] In fact, however, many of the Argo profile pairs (roughly 55%) do not show the expected intersection between pre-TC and post-TC profiles (as in Figures 8f, S2b, and S2c). In those cases, we have estimated z_c as the max(MLD_2, MLD_1), where MLD_1 and MLD_2 are MLDs before and after TC passages, respectively, defined by the density-based criterion equivalent to the SST-T(Z = MLD) ≥ 0.5 °C [*Glover and Brewer*, 1988; *Kara et al.*, 2000]. There is no significant difference in our results when choosing z_c as the min(MLD_2, MLD_1). Our definition of z_c, i.e., max(MLD_2, MLD_1), avoids producing negative bias in ΔH_A and positive bias in ΔH_B because of cancellation of samples from various random state of the background variability, e.g., phase of internal gravity wave. For example, suppose the given temperature profile is the black line in Figure 4f and that there is a thermocline depth fluctuation as 20 m [e.g., *Bond et al.*,
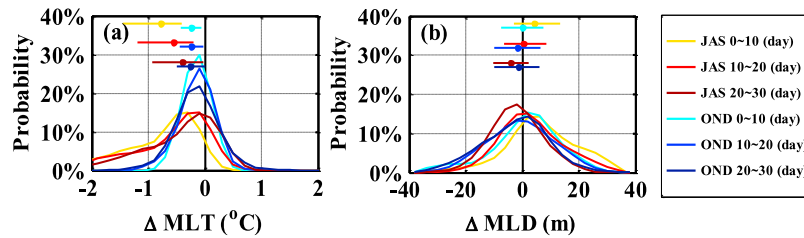
Figure 7. Probability density functions of (a) the mixed layer temperature difference and (b) the mixed layer depth difference (b) after TC events which represent responses solely due to the TCs estimated on the basis of deconvolution. Reddish colors are in warming season (July–September), and bluish ones are in cooling season (October–December). Each color stands for different time difference for each profile pair. The dots and horizontal lines show means and 25%–75% percentile ranges of corresponding PDFs.

2011]. The resultant bias would then be 0.05 GJ/m^2 if selecting z_c as either MLD$_1$ or MLD$_2$ for the nonintersecting pairs (see Figure S3). However, by choosing z_c as *max* (MLD$_2$,MLD$_1$), this bias becomes negligible.

[16] The deviation from the ideal, vertical mixing dominated case is likely due in part to background variability, which must be taken into account when using paired profiles from Argo floats to study TC response. The other reason of the deviation may be upwelling (upward vertical advection) near the track of a TC, which would be a case of cooling and a decrease of ΔH_B. Around 17% of the total samples were within 2 × RMW of the track, where upwelling may be important. The PDFs separated by upwelling and non-upwelling region are shown in Figure S4, although the analysis of basin-averaged heat content change includes all the samples. We note too that the results presented in section

3 are not sensitive to the lower depth (i.e., 400 m) chosen to estimate ΔH_B (discussed further in section 3).

[17] In order to test the significance of mean values of ΔH_A and ΔH_B, the standard error at 95% significance level (= $1.96\sigma/\sqrt{n}$) has been estimated, where mean (m) and standard deviations (σ) can be formulated by $m = \int xP(x)dx$ and $\sigma = \int (x - m)^2 P(x)dx$. Table 1 shows the mean values and standard errors of ΔH_A and ΔH_B.

2.5. Limitation of Data and Method

[18] There are three signals that the Argo profile pairs during TC periods measure: (1) Pure TC response is the heat content changes induced by TCs which we want to extract from the data. (2) TC-induced noise indicates the noise of the heat content changes generated by TC-induced high-frequency phenomenon, such as near-inertial oscillation and
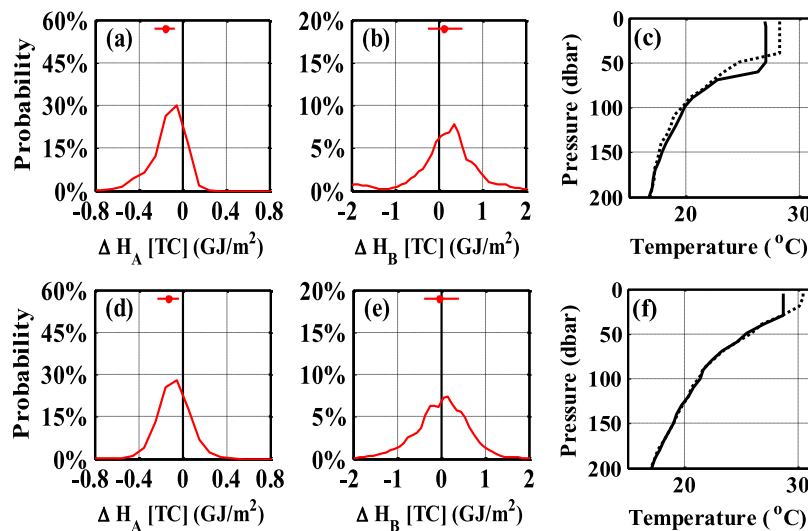

Figure 8. Probability density functions of estimated TC-induced responses (using deconvolution) of (a) near-surface (ΔH_A) and (b) subsurface (ΔH_B) heat content changes observed from the Argo profile pairs under strong TCs (greater than or equal to category 4). The dots and horizontal lines show means and 25%–75% percentile ranges of corresponding PDFs. (c) An example of temperature profile pairs (dotted lines, before TC event; solid lines, after TC event) obtained by the profiler ID 2900244 on 18 and 28 October 2003 during a strong TC (Typhoon Parma) passage (maximum sustained wind ∼59 m/s). (d and e) As in Figures 8a and 8b but for the Argo profiles under weak TCs (less than or equal to category 3). (f) An example of temperature profile pairs obtained by the profiler ID 5900189 on 11 and 21 September 2003 during a weak TC (MSW ∼ 18 m/s).

Table 1. Statistics of Heat Content Change Solely Induced by TCs[a]

	ΔH_A		ΔH_B	
	Warming Season	Cooling Season	Warming Season	Cooling Season
0–10 (day)	-0.10 ± 0.01	-0.02 ± 0.01	-0.04 ± 0.04	-0.04 ± 0.05
10–20 (day)	-0.10 ± 0.01	-0.02 ± 0.01	0.04 ± 0.06	-0.08 ± 0.10
20–30 (day)	-0.08 ± 0.01	-0.02 ± 0.01	0.04 ± 0.06	-0.05 ± 0.09

[a]Mean and its 95% significance level ($1.96\sigma/\sqrt{n}$), where σ is standard deviation and n is the number of profile pairs during TC events, in the near-surface (ΔH_A) and subsurface (ΔH_B) are calculated for three different time windows after the TC passage and for the warming and cooling seasons, respectively. The unit is GJ/m² (10^9 J/m²).

upwelling/downwelling. (3) Background variability is the noise due to background variability irrelevant to TC responses, such as seasonal cycle, internal tides, mesoscale eddies, and internal waves. The background variability, P_{BG}, is presumably independent of the TC-induced heat content change, P_{TC}, and can be separated from the observed P_{TC+BG} using the deconvolution method as already discussed in section 2.3. Nevertheless, analysis is done separately for the warm and cold season because both the TC statistics and the background variability exhibit apparent seasonal dependence.

[19] Differently from the background variability, due to limited temporal resolution of Argo data, the TC-induced noise cannot be directly removed from the observed P_{TC+BG} or the deconvoluted P_{TC}^*. However, the unresolved TC-induced high-frequency phenomena are unbiased, i.e., that they do not affect the estimated mean values but will increase the uncertainty of the estimated mean. One may concern that the upwelling expected along a TC track could induce a mean bias in the PDFs. For example the insignificant mean cooling in the profile of Figure 6f may be attributed to upwelling. Upwelling possibly causes a negative heat content change especially for the vertically integrated heat content, which may dominate over the heat content changes induced by the entrainment, especially at locations near the TC track (see Figure S4b). If upwelling dominates the heat content changes, especially the ΔH_B, the cooling signal should be greater with greater depth range of vertical integration. For example, in the single float data in the later half in Figure 4b, the integration depth dependency of ΔH_B appears to be significant.

[20] However, even when a substantially smaller depth range is used for the integration, i.e., $z_c = 200$ m instead of 400 m, the major results are unchanged, though the width of $P(\Delta H_B)$ becomes smaller (see Figure S5). Also, the upwelling should be balanced by downwelling over the greater area outside of RMW. The search radius, R_{17} encompasses the RMW of which the mean is ~40 km. Most importantly, even considering just the samples outside of the likely upwelling region, the mean values of ΔH_B are still insignificant (see Figure S4d). Therefore, we expect that the negative (cooling) biases in the PDFs associated with upwelling near a track are not large enough to change the main conclusions reached in this analysis.

[21] The Argo profile pairing method employed here has a limitation in the analysis of longer-term variation, >30 days,

because the number of samples meeting the sampling criteria becomes dramatically reduced. Most of the Argo floats considered in this study moved slowly enough to stay within 200 km window within 30 days, especially in the subtropical gyre. However, this is not necessarily true for a longer time window. Hence, we limit our analysis to the periods shorter than 30 days from the TC passages.

[22] Last, the PDF-based approach assumes that the sampled PDF is close to the true PDF. Assuming that there are enough data in regularly spaced grids, a PDF from randomly sampled data like Argo floats could approach the true PDF as the number of samples grows. Monte Carlo experiments with random samples using numerical simulations of the 3-D Price-Weller-Pinkel (PWP) model [*Price et al.*, 1986] suggest that more than 600 samples are required to achieve less than 20% of RMS differences in each PDF (not shown). All the PDFs shown here were constructed from more than 600 samples, and hence are believed to be fairly robust in this statistical sense. However, the 3-D PWP sampling exercise only considers the effect of the TC-induced noise on the PDF, but not that of the background variability. It is noted that about 6100 samples on average are used for estimating each PDF of background variability during non-TC events. Experiments of random resampling the above samples suggest that 600 samples also provide robust PDFs of background variability within about 5% of RMS difference from the PDFs obtained from the entire full sample. This apparent difference in the RMS resulting from 600 samples implies that an accurate estimation of the TC-induced noise requires more samples than that of the background.

3. Observations of Ocean Heat Content Changes Uptake

3.1. Necessity of Considering Background Variability

[23] Before describing the basin-averaged heat content change from all TC events, we first demonstrate the need for the deconvolution approach. Top two rows of Figure 6 present the PDFs of the various heat content anomalies observed from the Argo profile pairs. The first row exhibits the changes from the pairs observed during the periods of TCs, which reflects a sum of background and TC-induced variability, P_{TC+BG}. On the other hand, the second row shows the changes from the pairs independent of TCs (obtained by applying the same search criteria to the Argo profiles except for the periods without TC), which reflects the background variability, P_{BG}. In addition, the third row shows the PDFs of the estimated heat content changes induced by the TCs, P_{TC}, which are calculated on the basis of the deconvolution of the PDFs from the top two rows. The PDFs are further categorized into observations from the warming season (July–September) and the cooling season (October–December).

[24] Comparisons among the PDFs for the near-surface heat content changes (ΔH_A) (Figures 6a, 6c, and 6e) clearly illustrate the need for the deconvolution procedure. When only P_{TC+BG} is considered (Figure 6a), the PDFs in the cooling season (i.e., the lines with cool colors) are shifted toward the negative values, i.e., cooling, with greater extent than the ones in the warming season. This difference becomes more apparent as the time interval increases,

suggesting a secular trend, i.e., the seasonal cycle. Two additional PDFs, i.e., P_{BG} and P_{TC}, show that the warming and cooling due to the large 'background' seasonal cycle is indeed responsible for this trend. The estimated time rates of the heat content changes in Figure 6c are about -81 W/m^2 in the cooling season and $+39$ W/m^2 in the warming season, which are closely comparable to the NCEP–NCAR reanalysis I climatological surface heat fluxes of -81 W/m^2 and $+31$ W/m^2 for the respective season averaged over the domain (120°E∼180°, 5°N∼30°N) (despite that the Argo data distribution is inhomogeneous, Figure 3c).

[25] Also note that the widths of the PDFs are always larger in P_{TC+BG} and P_{BG} than P_{TC}. Once the background variability is removed, the PDFs of the estimated TC-induced response (P_{TC}) exhibit relatively narrower shapes. Thus, the deconvolution method evidently removes not only the bias induced by the seasonal cycle but also the increased spread caused by background variability. Thus the deconvolution method decreases the uncertainty in the estimated mean values of the TC-induced response. Furthermore, the reduced width of the PDF after the deconvolution process highlights that the heat content change due to the seasonal cycle, mesoscale or frontal features, will be often be larger than the variability of heat content change induced by TC and hence must be taken into account in some fashion.

3.2. TC-induced Near-Surface Heat Content Change ($P_{TC}(\Delta H_A)$)

[26] From now on, we will focus primarily on P_{TC}, the estimated TC-induced changes of heat content. In Figure 6e, $P_{TC}(\Delta H_A)$ exhibits significant negative mean values (dots superimposed in each panel of Figure 6) comparable to the widths at 95% confidence level (Table 1). This shows the expected cooling of the surface layer of the ocean. On the contrary, $P_{TC}(\Delta H_A)$ does not show a mean value significantly different from zero in any of the estimated PDFs (Figure 6f and Table 1) (more on this in section 3.3). Hence, we do not detect a significant warming at depth on average over all TC events analyzed here.

[27] Notice that the width of $P_{TC}(\Delta H_A)$ is 2–4 times smaller than that of the $P_{TC}(\Delta H_B)$. The difference may be associated with the difference in the dominant spatial scales between the TC responses at the near-surface and subsurface layers. The spatial scale of atmospheric forcing, which is large enough for the Argo pair sampling to resolve, likely set the dominant spatial scale for ΔH_A in the near the surface. On the other hand, the spatial scale for the ΔH_B or other subsurface quantities may be dominated by TC-driven oceanic processes which have smaller oceanic submesoscales or mesoscales (O(10–100 km)). Therefore, the pair sampling of Argo profiles likely provides more accurate information on PDFs of the mixed layer or near-surface than of the deeper, subsurface response. Due to the limitation on the number of Argo profiles, it is not practical to reduce the spatial search radius to better resolve the subsurface response.

[28] The near-surface cooling is greater in the warming season than in the cooling season. The relatively weak cooling of H_A in the cooling season may be attributed to the relatively colder MLT and deeper MLD of the pre-TC profiles compared to the warming season. Also, relatively weaker TCs in the cooling season can lead to the weaker

changes of H_A. Since the responses are generally greater in the warming seasons, we will mostly focus on the warming season for the further discussion below.

3.2.1. Slow Restoration of TC-Induced Near-Surface Ocean Heat Content

[29] Note that the $P_{TC}(\Delta H_A)$ is almost invariant in time after the TC passage (Figure 6e), in clear contrast to the P_{BG} (ΔH_A) (Figure 6c), which shows a very clear signal consistent with the seasonal cycle. This apparent the invariance of P_{TC} (ΔH_A) seems to imply that the restoration of the near-surface heat content (ΔH_A) is dominated mainly by the background seasonal cycle of the surface heat flux in the warming season (Figure 6c), and that any additional heat exchange generated in response to TCs is small enough to be undetectable in this analysis. If ΔH_A were completely restored to the prestorm condition between 10 and 30 days after a TC event, the PDFs should have shifted toward zero with time. Therefore the near-invariant PDFs of ΔH_A suggest that the restoration time scale is longer than 30 days (i.e., the maximum value used for the post-TC profile search). Previous studies have reported that the restoring time scale for SST ranges from 5 to 20 days (as seen in satellite data [e.g., *Hart et al.*, 2007; *Price et al.*, 2008]). If ΔH_A were restored as quickly as SST, the PDFs of ΔH_A would have presented noticeable shifts toward zero within the time frame of 30 days. As speculated by *Emanuel* [2001] and *Price et al.* [2008], it appears that the restoration time scale for ΔH_A must be substantially longer than that of the SST.

3.2.2. Fast Restoration of the Mixed Layer Temperature

[30] In order to clarify physical meaning of the near-invariant $P_{TC}(\Delta H_A)$, the temporal evolutions of ΔMLT and ΔMLD (i.e., surface properties) due to TC passages were investigated using the same Argo profile pairs and deconvolution method. In contrast to the negligible temporal evolution of ΔH_A, the MLT in the warming season evolves back toward the pre-TC condition (ΔMLT goes to zero) and MLD becomes shallower within 30 days (Figure 7). It appears that surface mixed layer formed as a part of the restratification after the TC event is generally shallower than the pre-TC mixed layer. Thus, the ΔMLT represents the changes within a comparatively thin surface layer, unlike ΔH_A which roughly applies over about 10–20 m (as schematically shown in Figures 1c and 1d). This result suggests that once the surface layer warms up, the slightly deeper subsurface layer that dominates ΔH_A may be effectively insulated from the atmosphere and will remain a cool anomaly until being exposed to the atmosphere in the following winter. On the contrary, in the cooling season, it is hard to identify any restoration of MLT (Figure 7a); that is, there is little or no warming of MLT in the cooling season.

3.3. TC-Induced Subsurface Heat Content Change ($P_{TC}(\Delta H_B)$)

[31] Now we will move on to the changes in the subsurface, ΔH_B. As pointed out already, the PDFs of the ΔH_B (Figure 6f) exhibit greater width compared to those of the ΔH_A and their means are not significantly different from zero. This has an important implication for the effort to estimate the global TC-induced OHU. Previous studies

inferred ΔH_B from satellite SST based on the assumption ΔH_B being comparable to ΔH_A as discussed in the introduction [e.g., *Sriver and Huber*, 2007]. However, the Argo observations suggest that the mean magnitudes of ΔH_B in the warming seasons (when ΔH_A shows significant cooling) are smaller than those of the ΔH_A (Table 1). A possible reason for this discrepancy may be that the ocean response to a strong TC and a weak TC may differ as discussed further below.

[32] Previous observational studies on the vertical structure of ocean response to TCs have emphasized mainly rather strong storms whose central pressures are less than 940 mb, equivalent to category 3. These studies have shown uniformly that an SST cold wake is due mainly to the entrainment process (enhanced vertical mixing). That results in comparable amplitudes of near-surface cooling (ΔH_A) and subsurface warming (ΔH_B) [*Price*, 1981; *D'Asaro et al.*, 2007], which has been a primary assumption of the OHU hypothesis [*Emanuel*, 2001; *Sriver and Huber*, 2007].

[33] Figures 8a and 8b present PDFs of ΔH_A and ΔH_B induced by strong TCs only (>58 m/s, stronger than category 4) which are obtained from Argo profiles. The $P_{TC}(\Delta H_A)$ and $P_{TC}(\Delta H_B)$ are significantly shifted toward negative and positive, respectively; the averages of ΔH_A and ΔH_B are -0.16 ± 0.01 GJ/m^2 and $+0.14 \pm 0.06$ GJ/m^2, where the uncertainties are at the 95% significance level. The comparable amplitudes of the two heat content changes indicate the dominance of entrainment process as the previous studies reported. A profile pair is shown in Figure 8c as an example for this strong storm (Typhoon Parma) case. On the contrary, the Argo profile pairs under weak TCs' influence show an insignificant mean, -0.03 ± 0.05 GJ/m^2, of $P_{TC}(\Delta H_B)$ in Figure 8e, though $P_{TC}(\Delta H_A)$ (the near-surface cooling) has clear negative shifts, -0.12 ± 0.01 GJ/m^2, in Figure 8d. An example of a profile pair under a weak storm (MSW $\sim$ 18 m/s) in Figure 8f suggests that the ML does not penetrate into the upper thermocline, often called a nonpenetrative convection. It appears that weak TCs do not produce strong penetrative mixing, but nevertheless, remove heat through the ocean surface and produce significant SST cooling; the high temporal resolution data of Figure 4 are an example. The magnitudes of ΔH_A ($\sim -0.20 \pm 0.01$ GJ/m^2) in the weak TC subsample (Figures 4d–4f) is larger than ΔH_B ($\sim +0.06 \pm 0.04$ GJ/m^2), while, in the strong TC case, $\Delta H_A = -0.09 \pm 0.01$ (GJ/m^2) and $\Delta H_B = +0.08 \pm 0.04$ (GJ/m^2) (Figures 4a–4c) are quite comparable. The heat content changes in the strong and weak TC cases are estimated by time averaging for 3 aliased inertial periods of 10.2 days and 13.8 days, respectively, after a TC passage in order to remove the effects of near-inertial upwelling and downwelling. Note that each ΔH_A here may contain seasonal heat loss to the atmosphere which reaches -5 W/m^2 in the strong TC case and -70 W/m^2 in the weak TC case on the basis of climatological data corresponding to the time-averaged heat loss of -0.001 GJ/m^2 and -0.04 GJ/m^2, respectively. Since computation of ΔH_B is sensitive to the integration depth range, especially in the strong storm case as addressed in section 2.5, the lower integration depth was set to 200 m for the both cases.

[34] The strong storms make up only about 14% of the total samples (Figure 2a). Therefore, basin-averaged ocean responses to all TC events are dominated by weak storm in which the entrainment process appears not to dominate the upper ocean temperature changes.

4. Summary and Discussion

4.1. Summary

[35] We have introduced a new approach to estimating the TC-induced changes in the upper ocean properties observed from Argo profiles pairs. A deconvolution of PDFs (probability density function) of the observed changes from TC and non-TC periods is used to estimate the PDFs of the TC-induced changes. Since TCs are episodic events, it was possible to estimate PDFs of the background variability independent of TC response. We have applied this new method to a study of the near-surface and subsurface ocean heat content changes in response to the TCs in the western North Pacific during 2000–2008. We have distinguished the TC-induced heat content changes in the warming season and in the cooling season to understand the impact of the background seasonal evolutions in the upper ocean. We have also examined the TC-induced changes for the three different periods after the TC passage, i.e., 0–10 days, 10–20 days, 20–30 days after the TCs, to investigate the restoring phase.

[36] Analysis of the TC-induced heat content changes suggests that the near-surface cooling (ΔH_A) induced by TCs is prominent in the warming season, but the corresponding subsurface heat content change (ΔH_B) caused by TC does not exhibit warming comparable to the magnitude of the near-surface cooling. This result is at odds with the assumption made in previous studies regarding TC-induced OHU that $\Delta H_B = -\Delta H_A$. We have shown that this assumption does, however, hold with the strong TCs ($\geq$ category 4 Typhoon). A possible reason for the mismatch between ΔH_A and ΔH_B found in the Argo observations is discussed in section 4.2 with details.

[37] Additionally, the time invariant PDFs of the near-surface heat content changes suggest that restoration of the near-surface cooling takes longer than 30 days, This is unlike the SST restoration time scale, which has been reported to be 5–20 days [*Hart et al.*, 2007; *Price et al.*, 2008]. Our analysis of surface mixed layer properties (Figure 5) also shows this comparatively fast restoration and suggests that the restoring of SST reflects only a thin near-surface layer, O(10 m), while a relatively slow restoring may follow in the rest of the near-surface layer, as shown schematically in Figure 1c. This is another important deviation from the assumptions made in previous TC-induced OHU studies.

4.2. Average Ocean Response Based on Argo Float Data

[38] A vertical mixing–dominated response results in an equivalent H_B warming and H_A cooling, as shown schematically in Figure 1a. The present results suggest that this is typical for strong TCs (category 4, MSW > 58 m/s, about 14% of the present data set, Figures 8a and 8b), as previous observational studies have shown. On the other hand, the response to weak TCs ($\leq$ category 3 and about 86% of the present data) exhibit small subsurface heat content changes that are not clearly different from zero in the Argo data set.

This implies nonpenetrative or weakly penetrative convection, perhaps resulting from a slightly enhanced case of regular mixed layer dynamics. Even in case the TCs are not strong enough to drive significant vertical mixing, they still extract heat from the ocean surface via latent heat flux, in which case the mean magnitude of ΔH_A would be larger than that of ΔH_B. In other words, the dominant mechanisms of the near-surface cooling seem different for strong and weak TCs.

[39] TC category 3 is not a definite threshold to separate between responses dominantly due to vertical entrainment and due to comparable contributions from air-sea heat exchange and entrainment. Probably, TC parameters as well as oceanic environmental conditions, e.g., stratification, are important factors to determine the relative contributions between the two. It should be revealed by further thorough studies why and how the relative contribution is determined. Another surprising result is that the near-surface cooling induced by the strong TCs are only 25% greater than by weak TCs as shown in Figure 8. It is uncertain why the difference of the cooling by the strong and weak TCs are not greater. The question is also remained as a future study.

[40] On the basis of the results in this study, we propose a schematic of the basin-averaged ocean response to TCs in the North Pacific, especially for the warming season in Figures 1c and 1d modified from Figure 1a assumed by the previous TC-induced OHU studies. As an immediate response to a TC passage, near-surface heat content is cooled with larger magnitude than warming in the subsurface as shown in Figure 1c. In the following several weeks, only a rather thin surface layer is restored, while the rest of the cooled near-surface heat content remains unrestored, as in Figure 1d.

4.3. Comparison With the Previous TC-Induced OHU Studies

[41] The magnitude of ΔH_A from the $P_{TC}(\Delta H_A)$ (Table 1) is comparable to the estimates of surface layer cooling from previous studies. -0.1 GJ/m^2 of ΔH_A, which corresponds roughly to 0.5°C cooling within an MLD of 50 m. In order to make rough comparisons with the previous TC-induced OHU values, this mean ΔH_A is integrated over the area along the TC track, swath of 250 km (the average value of R17 in the North Pacific). Summed over the global ocean and divided by 1 year for an annual mean estimate, supposing that the mean ΔH_A in the North Pacific would represent the global mean (although the western North Pacific is the most energetic basin for TCs). The present estimate of TC-induced ΔH_A corresponds to very roughly -0.19 ± 0.03 PW. Under the assumption that ΔH_A is comparable to ΔH_B as in the previous studies, the order of the OHU is comparable to the previous ones estimated using satellite SST data [e.g., *Sriver et al.*, 2008; *Jansen et al.*, 2010]. However, as we have noted repeatedly, ΔH_B directly estimated from the profile pairs does not exhibit this magnitude of warming.

[42] Additionally, *Jansen et al.* [2010] pointed out that the only portion of the subsurface excessive heat (ΔH_B) survived from outcropping to the sea surface through the end of the following winter should be considered as the OHU in a climatological sense. If the post-TC MLD produced by TC-induced vertical mixing is deeper than the following winter's MLD, at least a portion of the ΔH_B can survive in the

subsurface without being exposed to the atmosphere and thus may be removed via the basin-scale ocean heat transport. Argo profile data can also be used to compare the post-TC MLD with the mean winter's MLD also estimated from Argo profiles in the region. About 86% of post-TC MLDs obtained from Argo data in the warming season is shallower than the winter MLD, even though ΔH_A in the warming season exhibit significant cooling (refer to Figure S6). In addition, about 62% of the post-TC MLD in the cooling is shallower than the winter MLD.

[43] In summary, an OHU uptake associated with the subsurface heat gain induced by TCs is not detectable in Argo profile measurements. Moreover, we have discussed several aspects of PDFs of the TC-induced heat content changes that appear not to support the TC-induced OHU hypothesis suggested in the previous studies and the assumptions made in those studies. These aspects include slow (>30 days) restoration of ΔH_A, and a mean magnitude of ΔH_B that is not different from zero.

References

Biggs, D. S. C., and M. Andrews (1997), Acceleration of iterative image restoration algorithms, *Appl. Opt.*, *36*(8), 1766–1775, doi:10.1364/AO.36.001766.

Bond, N. A., M. F. Cronin, C. Sabine, Y. Kawai, H. Ichikawa, P. Freitag, and K. Ronnholm (2011), Upper ocean response to Typhoon Choi-Wan as measured by the Kuroshio Extension Observatory mooring, *J. Geophys. Res.*, *116*, C02031, doi:10.1029/2010JC006548.

Cornillon, P., L. Stramma, and J. F. Price (1987), Satellite measurements of sea surface cooling during Hurricane Gloria, *Nature*, *326*, 373–375, doi:10.1038/326373a0.

D'Asaro, E. A., T. B. Sanford, P. P. Niiler, and E. J. Terrill (2007), Cold wake of Hurricane Frances, *Geophys. Res. Lett.*, *34*, L15609, doi:10.1029/2007GL030160.

Dean, L., K. A. Emanuel, and D. R. Chavas (2009), On the size distribution of Atlantic tropical cyclones, *Geophys. Res. Lett.*, *36*, L14803, doi:10.1029/2009GL039051.

Emanuel, K. (2001), Contribution of tropical cyclones to meridional heat transport by the oceans, *J. Geophys. Res.*, *106*, 14,771–14,781, doi:10.1029/2000JD900641.

Glover, D. M., and P. G. Brewer (1988), Estimates of wintertime mixed layer nutrient concentrations in the North Atlantic, *Deep Sea Res., Part A*, *35*, 1525–1546, doi:10.1016/0198-0149(88)90101-X.

Hart, R. E., R. N. Maue, and M. Watson (2007), Estimating local memory of tropical cyclones through MPI anomaly evolution, *Mon. Weather Rev.*, *135*, 3990–4005, doi:10.1175/2007MWR2038.1.

Hirschman, I. I., and D. V. Widder (1955), *The Convolution Transform*, 288 pp., Princeton Univ. Press, Princeton, N. J.

Jansen, M. F., R. Ferrari, and T. A. Mooring (2010), Seasonal versus permanent thermocline warming by tropical cyclones, *Geophys. Res. Lett.*, *37*, L03602, doi:10.1029/2009GL041808.

Kara, A. B., P. A. Rochford, and H. E. Hurlburt (2000), An optimal definition for ocean mixed layer depth, *J. Geophys. Res.*, *105*(C7), 16,803–16,821, doi:10.1029/2000JC900072.

Kwon, Y.-O. (2003), Observation of general circulation and water mass variability in the North Atlantic Subtropical Mode Water region, Ph.D. thesis, Univ. of Wash., Seattle.

Liu, Z., J. Xu, B. Zhu, C. Sun, and L. Zhang (2007), The upper ocean response to tropical cyclones in the northwestern Pacific analyzed with Argo data, *Chin. J. Oceanogr. Limnol.*, *25*(2), 123–131, doi:10.1007/s00343-007-0123-8.

Park, J. J., and K. Kim (2007), Evaluation of calibrated salinity from profiling floats with high resolution conductivity-temperature-depth data in the East/Japan Sea, *J. Geophys. Res.*, *112*, C05049, doi:10.1029/2006JC003869.

Park, J. J., K.-A. Park, K. Kim, and Y.-H. Youn (2005), Statistical analysis of upper ocean temperature response to typhoons from ARGO floats and satellite data, in *Geoscience and Remote Sensing Symposium, IGARSS '05, Proceedings, 2005 IEEE International*, 2564–2567, Inst. of Electr. and Electron. Eng., Piscataway, N. J., doi:10.1109/IGARSS.2005.1525508.

Pasquero, C., and K. Emanuel (2008), Tropical cyclones and transient upper-ocean warming, *J. Clim.*, *21*, 149–162, doi:10.1175/2007JCLI1550.1.

Price, J. F. (1981), Upper ocean response to a hurricane, *J. Phys. Oceanogr.*, *11*, 153–175, doi:10.1175/1520-0485(1981)011<0153:UORTAH>2.0.CO;2.

Price, J. F., R. A. Weller, and R. Pinkel (1986), Diurnal cycling: Observations and models of the upper ocean response to diurnal heating, cooling, and wind mixing, *J. Geophys. Res.*, *91*(C7), 8411–8427, doi:10.1029/JC091iC07p08411.

Price, J. F., J. Morzel, and P. P. Niiler (2008), Warming of SST in the cool wake of a moving hurricane, *J. Geophys. Res.*, *113*, C07010, doi:10.1029/2007JC004393.

Sanford, T. B., J. F. Price, J. B. Girton, and D. C. Webb (2007), Highly resolved observations and simulations of the ocean response to a hurricane, *Geophys. Res. Lett.*, *34*, L13604, doi:10.1029/2007GL029679.

Shi, W., and M. Wang (2011), Satellite observations of asymmetrical physical and biological responses to Hurricane Earl, *Geophys. Res. Lett.*, *38*, L04607, doi:10.1029/2010GL046574.

Sriver, R. L., and M. Huber (2007), Observational evidence for an ocean heat pump induced by tropical cyclones, *Nature*, *447*, 577–580, doi:10.1038/nature05785.

Sriver, R. L., M. Huber, and J. Nusbaumer (2008), Investigating tropical cyclone-climate feedbacks using the Tropical Measuring Mission (TRMM) microwave imager and the quick scatterometer, *Geochem. Geophys. Geosyst.*, *9*, Q09V11, doi:10.1029/2007GC001842.

Y.-O. Kwon, J. J. Park, and J. F. Price, Physical Oceanography Department, Woods Hole Oceanographic Institution, 266 Woods Hole Rd., Woods Hole, MA 02543, USA. (jjpark@whoi.edu)